

# Assessment of the decadal morphodynamic evolution of a mixed energy inlet using ocean color remote sensing

Sylvain Capo · Bertrand Lubac · Vincent Marieu ·  
Arthur Robinet · Driss Bru · Philippe Bonneton

Received: 2 December 2013 / Accepted: 9 August 2014  
© Springer-Verlag Berlin Heidelberg 2014

**Abstract** A consistent time series of synoptic and high-frequency bathymetric observations is fundamental to improving our understanding and predictive capabilities regarding the morphological behavior of large coastal inlets. Based on satellite observations, an original approach is proposed to characterize the long-term morphological evolution of the Arcachon lagoon inlet and to describe sediment bypassing and breaching mechanisms. The almost 26-year-long remotely sensed data archive used in this study is built from 78 suitable SPOT images (1986–2012) collected in the framework of the KALIDEOS-Littoral program. Bathymetric information is derived from satellite data using a physics-based model. A validation exercise performed on a large bathymetric survey data set ( $N=43,949$ ) demonstrates that the inversion model performs excellently in estimating the depth of mildly to moderately turbid shallow waters. The performance of the model suggests that the minimum requirements are fulfilled to apply the SPOT-derived bathymetry to morphodynamic applications. We demonstrate that high-spatial-resolution multi-spectral sensors are well adapted to analyzing the morphological evolution of small- (i.e., sand dunes), medium- (i.e., sandbanks and channels), and large- (i.e., the entire inlet-

lagoon system) scale sedimentary structures present in coastal inlets. For the first time, the long-term evolution of a flood and ebb-tidal delta is characterized by observations at a seasonal timescale. Finally, migration rates of sedimentary entities are quantified, and fundamental mechanisms driving the sediment transport cross the inlet are confirmed.

**Keywords** Ocean color · Multispectral · Radiative transfer-based model · Bathymetry · Morphodynamics · Inlet

## 1 Introduction

Knowledge on the temporal and spatial morphological evolution of coastal systems is of great interest for marine engineering sciences. For instance, ecosystem-based management and ecological risk assessment within coastal area require accurate and up-to-date information on the nearshore morphology. This information is crucial to correctly model the vulnerability of hinterland to flooding events (Gesch 2009) and the resident times in estuarine and lagoon environments and predict the nearshore ocean wave and current (Van Dongeren et al. 2008; Holman et al. 2013). Morphological changes are driven by complex feedback systems, including the hydrodynamics of tidal currents combined to wind waves and the sediment transport via erosion and deposition mechanisms induced by hydrodynamics and bottom morphology (De Swart and Zimmerman 2009). Due to the complexity of these physical processes, assessment of the morphological behavior of coastal systems remains a daunting task.

Among the different existing coastal environments, mixed energy tidal inlets (Hayes 1979) most likely represent the most extreme level of difficulty in terms of nearshore flow and sediment transport modeling. In these environments, the physical forcing controlling the significant bathymetric changes at decadal time scales is well identified: storm intensity and

---

Responsible Editor: Aldo Sottolichio

This article is part of the Topical Collection on the *7th International Conference on Coastal Dynamics in Arcachon, France 24-28 June 2013*

S. Capo · B. Lubac (✉) · D. Bru  
UMR 5805 EPOC, Université de Bordeaux, Allée Geoffroy  
St-Hilaire, Pessac 33615, France  
e-mail: b.lubac@epoc.u-bordeaux1.fr

S. Capo  
Telespazio, Izarbel, 64210 Bidart, France

V. Marieu · A. Robinet · P. Bonneton  
UMR 5805 EPOC, CNRS, Allée Geoffroy St-Hilaire, Pessac 33615,  
France

frequency, sea level trends, wave climate, tidal range, sediment supply, and geological settings (Woodroffe 2003). However, the identification of their respective roles is still hampered by a lack of both forcing and geomorphological data (Viles and Goudie 2003). To improve our understanding of the physical processes driving these morphological changes, studies using complementary approaches (i.e., observation, laboratory experimentation, and modeling) have to be conducted.

Numerical studies attempt to consider realistic forcing to accurately reproduce the morphodynamic evolution predicted by conceptual models. Thus, long- to medium-term simulations performed in idealized (van Leeuwen et al. 2003; Dissanayake et al. 2009; de Swart and Zimmerman 2009) or specific tidal inlet systems (Dastgheib et al. 2008; Wang et al. 2012) have led to a better understanding of the mechanisms controlling the development of the main sedimentological structures and general morphologies of such systems. In particular, physical processes responsible for channel and bank evolution have been investigated in detail using process-based models forced by realistic wave and tide conditions for short- (Williams and Pan 2011; Bertin et al. 2009) to long-term scales (Cayocca 2001; Nahon et al. 2012; Plecha et al. 2012). The impact of the tidal asymmetry and the ebb dominance on the channel development was analyzed by Bertin et al. (2009). Nahon et al. (2012) confronted empirical theories with results obtained from numerical simulations and reproduced the conceptual model of sand bypassing by ebb delta breaching. Cayocca (2001) developed a morphodynamic model of the Arcachon lagoon inlet to give “better insight into the respective roles of tides and waves in driving the morphological changes of this mixed energy inlet.” Results highlighted the dominant role of tides to explain the opening of new channels and waves to control the direction of migration of the sandy structures and channels across the inlet.

As shown by the studies previously cited, validation of the results of numerical simulations and thus development of conceptual theories dramatically depend on the quality of observations. In particular, the temporal and spatial resolutions are critical to address small-scale morphodynamic mechanisms. Concerning the morphological evolution of the Arcachon lagoon inlet, the current empirical conceptual model used by the scientific community was established by Gassiat (1989) and Michel and Howa (1997) from heterogeneous and large-scale data. This model links ebb delta dynamics to adjacent shorelines. Authors suggest a two-stage cycle with an approximately 80-year-long period mainly driven by the wave-induced southward littoral drift. The first stage of this cycle presents two functioning channels. Both channels progressively migrate toward the south, and the NC eventually merges with the southern channel. The second stage presents only one functioning channel which is associated to a large growing of the ebb delta located between the sandy spit and

the southern single channel. The need for regular data at high temporal and spatial scales is crucial to improve this large-scale model and in particular to improve the description of bypassing and breaching mechanisms and the quantification of the sediment transport and sand structure migration rates.

Remote sensing of ocean color from space sensors is a relevant tool for that purpose and has to be thought in terms of complementarity in the perspective of integrated multisource observation systems. Traditional bathymetric monitoring techniques, such as echo soundings, light detection and ranging (LIDAR), and hyperspectral airborne surveys, are widely used to obtain accurate bathymetries, but the cost of these solutions for large and energetic coastal environments is prohibitive for high-frequency monitoring (Minghelli-Roman et al. 2009). Satellite-borne multispectral remote sensing is a cost-effective and relevant alternative to monitor morphological changes over large coastal areas despite higher uncertainties on the bathymetry product (Su et al. 2008; Dekker et al. 2011; Klemas 2011; Bramante et al. 2013). In particular, high-spatial-resolution sensors, such as SPOT sensors, PLEIADES, or SENTINEL-2, have the required revisit frequency and spatial resolution for this task (Dehouck et al. 2009; Lee 2010; Dekker et al. 2011).

The present paper aims at presenting an original quasi-analytical algorithm to retrieve the bathymetry from ocean color radiometry and assessing the potential of high-spatial-resolution sensors (HRS) to describe the morphological evolution and sedimentary transport mechanisms occurring in the Arcachon lagoon inlet. The bio-optical inversion model is validated on a large matchup data set then applied on the almost 26-year-long satellite archive of KALIDEOS. Morphological applications concern the quantification of migration rates of small- and large-scale sedimentary structures and the description of bypassing and breaching mechanisms. This study constitutes an important contribution to the understanding and validation of the morphodynamic processes in mixed energy inlet systems as a result of long-term observations acquired at high temporal and spatial resolutions.

## 2 Water depth inversion from ocean color radiometry

Most of the passive optical remote-sensing methods addressing the extraction of depth information are based on the analytical shallow water reflectance model initially proposed by Lyzenga (1978), improved by Philpot (1989) and Maritorena et al. (1994), and reformulated by Lee et al. (1999) and Albert and Gege (2006). According to this model, the subsurface remote-sensing reflectance,  $r_{rs}^{dp}$  (in  $\text{sr}^{-1}$ ), can be

approximated as a sum of contributions from the water column and from the bottom substrate:

$$r_{rs} = r_{rs}^{dp} [1 - A_1 \exp[-(K_d + k_u^{dp})H]] + A_2 R^B \exp[-(K_d + k_u^B)H] \tag{1}$$

where  $r_{rs}^{dp}$  (in  $\text{sr}^{-1}$ ) is the subsurface remote-sensing reflectance over hypothetical optically deep waters;  $K_d$  (in  $\text{m}^{-1}$ ) is the vertically averaged diffuse attenuation coefficient for downwelling irradiance;  $k_u^{dp}$  and  $k_u^B$  (in  $\text{m}^{-1}$ ) are the vertically averaged diffuse attenuation coefficient for upwelling irradiance originating from each layer of the water column and the bottom, respectively;  $R^B$  is the bottom albedo;  $A_1$  and  $A_2$  are constants depending on the scattering process in the water column and nature of the bottom, respectively; and  $H$  (in m) is the water depth. For multispectral applications, because the spectral band number is small compared to hyperspectral sensors, solving the inverse problem requires a decrease in the number of unknowns in Eq. 1. An approximate solution of the reflectance model for interpreting the radiative transfer over shallow waters is given by the following:

$$r_{rs} = r_{rs}^{dp} [A_1 - \exp(-2KH)] + A_2 R^B \exp(-2KH) \tag{2}$$

$A_1$  and  $A_2$  take the values 1 and  $1/\pi$ , respectively, assuming that the quasi-single scattering and the bottom are a Lambertian reflector.  $K$  (in  $\text{m}^{-1}$ ) is the vertically averaged effective or operational attenuation coefficient, which assumes no distinction between  $K_d$ ,  $k_u^{dp}$ , and  $k_u^B$ . In practice,  $K$  is replaced by  $K_d$ , which can be accurately estimated from ocean color data. Rearranging Eq. 2, we obtain the following well-known expression for  $H$  as a function of  $K$ ,  $R^B$  and  $r_{rs}^{dp}$ :

$$H = \frac{1}{2K} \left[ \ln \left( \frac{1}{\pi} R^B - r_{rs}^{dp} \right) - \ln(r_{rs} - r_{rs}^{dp}) \right] \tag{3}$$

This equation, with only three unknowns, is the foundation of most multispectral algorithms developed in the past few decades to retrieve water depth from ocean color radiometry. It is important to note here that Eq. 3 is not exact. As noted by Maritorena et al. (1994), “a safe use of such expression requires that the underlying approximations are acceptable and their impact quantified.” In particular, the impact of the  $K$  approximation on water depth retrieval has to be precisely analyzed. Maritorena et al. (1994) showed that setting  $k_u^{dp}$  and  $k_u^B$  equal to  $K_d$  results, in the case of particle-dominated scattering, in an overestimation of  $H$  ranging from 1 to 33 %. The results of Kirk (1991) and Lee et al. (1999) suggest a higher error on the computed water depth. However,

similarly to Lyzenga et al. (2006), under appropriate optical and boundary conditions, we believe that the “most familiar form” of the water depth inversion model (to refer to O’Neill and Miller 1989) is accurate enough for most applications.

Recent comparative studies (Su et al. 2008; Dekker et al. 2011; Bramante et al. 2013) confirm that standard multispectral methods (Lyzenga 1978; recently extended by Lyzenga et al. 2006; Stumpf et al. 2003) perform well and not significantly worse than hyperspectral methods (Dekker et al. 2011) in estimating water depth. Empirical approaches used in these methods allow partial compensation for variability in bottom reflectance and inherent optical properties (IOPs) of the water column across the image and correct the error associated with the  $K$  approximation. However, the performance of empirical methods dramatically depends on the representativeness of the training data set. This point becomes critical in the case of an analysis of a longtime series of ocean color observations where, in general, few images can be used to calibrate the empirical algorithms.

In this paper, the objective is to analyze the almost 26-year archive from KALIDEOS to identify long-term trends and quantify decadal changes in the morphology of coastal areas. Note that a limited number of observations are available to compose a training data set. To take into account the variability of the seasonal and inter-annual optical conditions, we propose an original quasi-analytical multispectral model for shallow water bathymetry inversion (QAB) based on published algorithms. Figure 1 presents the schematic flowchart of the QAB. A brief description of the various steps is given in the following of this section.

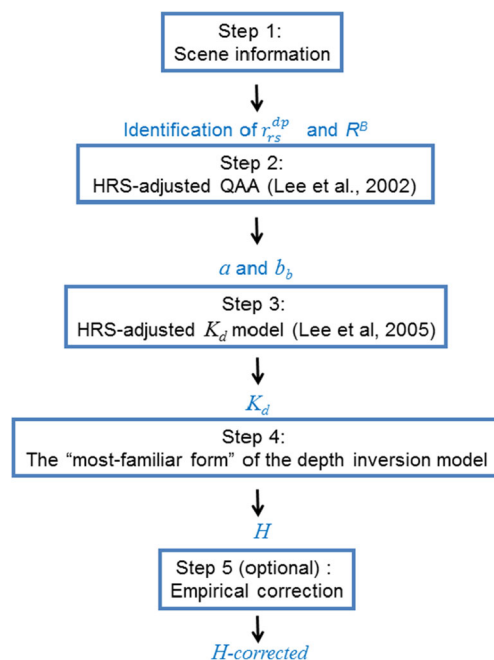


Fig. 1 Schematic flowchart of the QAB

Step 1 automatically extracts the bottom remote-sensing reflectance,  $R_{rs}^B = R^B/\pi$  (in  $\text{sr}^{-1}$ ) and the subsurface remote-sensing reflectance over optically deep waters,  $r_{rs}^{dp}$ , from the satellite scene. The algorithm to extract  $R_{rs}^B$  combines a normalized difference water index and a normalized humidity index. These two band ratio indices are used to define a mask that allows the identification of the wet sandy substratum reflectance. A visual check of the image is then performed to validate the result. The extraction of  $r_{rs}^{dp}$  is based on a computation of the mean of  $r_{rs}$  over an optically homogeneous specific area of the image in which the depth is great enough to avoid the impact of the bottom on the water-leaving signal. In this study, an area of the image is defined as optically homogeneous when the between-pixel variance equals the environmental noise equivalent reflectance difference,  $NE\Delta r_{rs}$ , calculated following the methodology of Wettle et al. (2004). Note that ocean color sensors measure the remote-sensing reflectance above the surface,  $R_{rs}$  (in  $\text{sr}^{-1}$ ). To compute  $r_{rs}$ , the following expression is used (Gordon et al. 1988):

$$r_{rs} = \frac{R_{rs}}{n_0 + n_1 R_{rs}} \tag{4}$$

where  $n_0$  and  $n_1$  are two constants that account for the effects of the water-air interface on the radiometric signal.

Step 2 derives the total absorption and backscattering coefficient at the reference wavelength ( $a(\lambda_0)$  and  $b_b(\lambda_0)$ ), respectively, in  $\text{m}^{-1}$  from  $r_{rs}^{dp}$ . The algorithm is based on the quasi-analytical algorithm (noted QAA; Lee et al. 2002) adjusted for HRS. Briefly, the QAA starts with the calculation of the total absorption coefficient using a nonlinear relationship between  $a(\lambda_0)$  and  $r_{rs}^{dp}$  at different wavelengths in the visible part of the electromagnetic spectrum:

$$a(\lambda_0) = f(r_{rs}^{dp}(\lambda_i), r_{rs}^{dp}(\lambda_j), \dots) \tag{5}$$

Next, the backscattering coefficient is derived using the following relationship:

$$u(\lambda_0) = \frac{b_b(\lambda_0)}{a(\lambda_0) + b_b(\lambda_0)} = \frac{-g_0 + \sqrt{g_0^2 + 4g_1 r_{rs}^{dp}(\lambda_0)}}{2g_1} \tag{6}$$

$g_0$  and  $g_1$  are two constants.

Step 3 derives the averaged diffuse attenuation coefficient for downwelling irradiance,  $K_d$ , using the model of Lee et al. (2005) adjusted for HRS:

$$K_d(\lambda_0) = m_0 a(\lambda_0) + m_1 [1 - m_2 \exp(-m_3 a(\lambda_0))] b_b(\lambda_0) \tag{7}$$

with  $m_0 \cong 1 + 0.005\theta_s$  and  $\theta_s$  as the solar zenith angle;  $m_1$ ,  $m_2$ , and  $m_3$  are constants.

Step 4 derives the water depth  $H$  using Eq. 3, where  $K$  is replaced by  $K_d$ . The accuracy and precision on computed  $H$  depend on two factors: errors in satellite measurements ( $R_{rs}$ ) and errors in assumptions regarding the QAB. Errors in  $R_{rs}$  are mainly introduced by inappropriate atmospheric corrections. Errors in model assumptions are largely explained by the  $K$  approximation. Because of the mathematical formulation of Eq. 3, the impact of the atmospheric corrections on the second term of the right expression,  $\ln(R_{rs}^B - r_{rs}^{dp}) - \ln(r_{rs} - r_{rs}^{dp})$ , can be assumed as negligible in comparison to the impact on the first term,  $1/2K$ . The total error (i.e., bias and noise) in  $H$  is therefore mainly explained by the error in  $K$ . This characteristic of the QAB represents a major point of interest to analyze and quantify the limits of the method and to empirically correct the bias if matchups are available. The empirical correction using a simple linear regression represents an optional step 5 of the QAB. The bias-corrected water depth,  $H_c$ , is given by the following expression:

$$H_c = \frac{\alpha}{2K} \left[ \ln\left(\frac{1}{\pi} R^B - r_{rs}^{dp}\right) - \ln(r_{rs} - r_{rs}^{dp}) \right] + \beta \tag{8}$$

where  $\alpha$  and  $\beta$  are two constants provided by the linear regression.

### 3 Data and method

#### 3.1 Site location

The Arcachon basin is located in southwest France on the Atlantic coast (Fig. 2, left panel). The basin is composed of a lagoon that is connected to the Atlantic Ocean through a large mixed energy inlet. The inlet exhibits many morphological sand units covering a large range of scales, from sand ripples to ebb and flood delta sandbanks. It is a single inlet composed of two relatively narrow, deep channels, approximately 1,000 m wide and up to 20 m deep (Fig. 2, right panel). The northern channel (NC) splits the ebb-tidal delta into two sedimentary entities: an upper ebb delta (UED), called the Toulinguet sandbank, and a lower ebb-tidal delta (LED) between NC and southern channel (SC), called the Arguin sandbank. Inward, the channel depth diminishes to 10–15 m, and shallow submerged sandbanks build up a flood-tidal delta (FD) with meandering morphology, which is attached north of the coast close to Arcachon City and is connected to the upper reach of the LED by a sand dune field (SDF) (see Fig. 2, right panel).

The Arcachon lagoon inlet is subject to meso- to macro-tidal conditions (i.e., approximately 4-m tidal range) and has

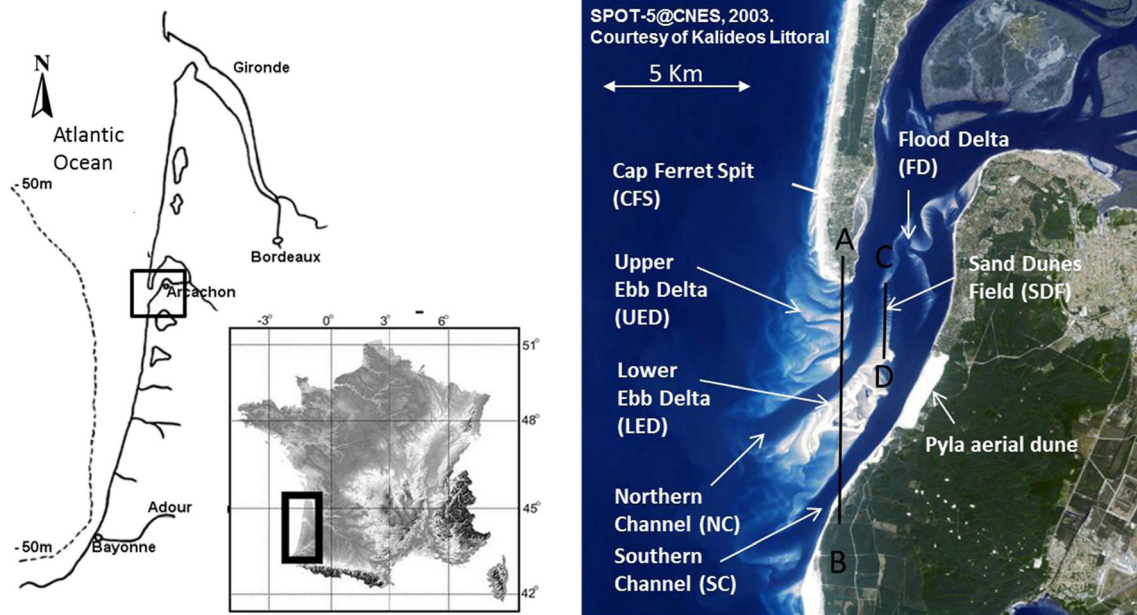


**Fig. 2** Location of the Arcachon basin in southwest France (*left*) and enlargement of the inlet (*right*) with indications of the principal sedimentary entities of the inlet and the two reference alongshore lines crossing the ebb tidal delta (slice AB) and the sand dune field (slice CD)

an energetic wave climate. The annual significant wave height is approximately 1.36 m (Butel et al. 2002). Extreme conditions are most frequently observed during winter storms, when waves can exceed 5 m in height. Optical conditions are associated with mildly to moderately turbid waters. The  $K_d$  values at 490 nm range from 0.30 to 0.95  $\text{m}^{-1}$ . The chlorophyll concentration varies from 0.21 to 2.80  $\text{mg m}^{-3}$  and the suspended particulate matter concentration from 1.44 to 11.09  $\text{g m}^{-3}$  (unpublished data). Optically shallow waters of the inlet, those in which the bottom radiometric signal “measurably influences”  $R_{rs}$  (Dekker et al. 2011), are uniformly covered by quartz sand material characterized by a cross section ranging from 200 to 400  $\mu\text{m}$  (Pedreros et al. 1996; Cayocca 2001). Boundary conditions associated with the sandy substratum are therefore characterized by a homogeneous bottom albedo and positive “bottom contrast.”

### 3.2 Acoustic bathymetry data

Bathymetric surveys are regularly conducted in the inlet of the Arcachon lagoon by the Direction Départementale des Territoires et de la Mer (DDTM) and the Syndicat Intercommunal du Bassin d’Arcachon (SIBA) for security purposes. Echo-sounding data were corrected for roll, pitch, yaw, and GPS latency. Next, the water depth data were standardized to the French Marine Height Datum (FMHD) to compute the acoustic bathymetry. The uncertainty in bathymetry was assumed to be less than 15 cm. Acoustic bathymetry data were used to empirically correct and validate the QAB. To ensure that in situ data were accurately coregistered with satellite data

at a pixel level, a resample of acoustic bathymetry was performed to match the pixel size of the remotely sensed image.

### 3.3 Image acquisition and processing

To investigate the long-term morphological evolution of the Arcachon basin inlet, satellite level-3 data are regularly acquired over the area in the frame of the KALIDEOS-Littoral program (<http://kalideos.cnes.fr/spip.php?article42>). The satellite scenes, composed of SPOT-1 to SPOT-5 images, were processed with the software package of KALIDEOS, which ensures homogeneity of treatment for all images (Lafrance et al. 2012). The data processing includes geometric and atmospheric corrections, with innovative treatments to remove the sun glint and adjacency effects. A strict control of image quality in terms of aerosol optical thickness, cloud-free atmosphere, and sea surface state conditions was performed to ensure an accurate inversion of the water depth.  $NE\Delta r_{rs}$  (Wettle et al. 2004) was used as objective criteria to validate the radiometric quality of the image. During the period from mid-1986 to late-2012, 78 images were selected, corresponding to a revisit frequency of approximately 0.3 images per month (Fig. 3).

### 3.4 SPOT-adjusted models

The QAA (Lee et al. 2002) and the  $K_d$  model (Lee et al. 2005) were initially developed for medium-spatial-resolution ocean color sensors such as SeaWiFS, MODIS, or MERIS. To apply these models to SPOT data, the algorithms needed to be

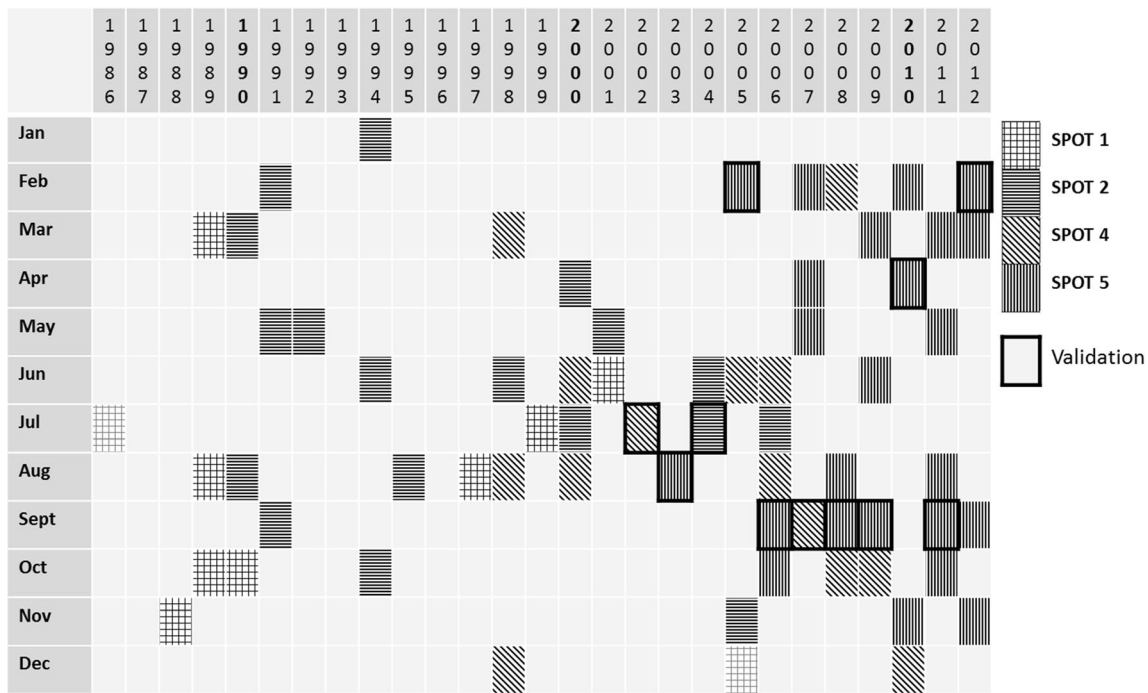


**Fig. 3** Distribution of the KALIDEOS-SPOT images used in this study. Textured cells indicate the presence of satellite data; grids are associated with SPOT-1, horizontal lines with SPOT-2, oblique lines with SPOT-4,

and vertical lines with SPOT-5. Cells with a thick contour line indicate images used for validation of the bathymetric inversion methods

adapted to take into account the spectral specificities of the sensor in terms of bandwidths and band number. In particular, a new formulation of Eq. 5 is proposed in this study:

$$a(\lambda_0) = a_w(\lambda_0) + p_0 \left( \frac{r_{rs}^{dp}(645)}{r_{rs}^{dp}(\lambda_0)} \right)^2 + p_1 \left( \frac{r_{rs}^{dp}(645)}{r_{rs}^{dp}(\lambda_0)} \right) + p_2 \tag{9}$$

where  $\lambda_0=545$  nm and  $a_w(\lambda_0)=0.05195\text{m}^{-1}$ . New coefficients for Eqs. 4, 6, 7, and 9 were computed using a simple least square fitting performed on synthetic data (IOCCG 2006). The synthetic data set used in this study is composed of the 1,000 simulations computed from the radiative transfer code HYDROLIGHT (Mobley 1994) for different bio-optical conditions and two different solar zenith angles (30° and 60°). Note that the mean annual solar zenith angle in the Arcachon basin associated with the time of SPOT passage is approximately 43°, with a maximum value of 65° and a minimum value of 20°. Values of the coefficients are given in Table 1.

The optimization scheme has led to a slight modification of the values of the constants in Eqs. 4 and 6, which are independent of the wavelength. As expected, the adjusted models did not perform significantly better. For Eq. 4, the root mean square error (RMSE) between the synthetic and inverted  $r_{rs}$  using the published coefficient is 0.0012 compared to 0.0008 with the new coefficients. For Eq. 6, the RMSE is 0.0046

versus 0.0048. In contrast, the new coefficients for Eqs. 7 and 9, which are wavelength-dependent, dramatically improve the performance of the models (see RMSE values in Table 1).

### 3.5 Satellite bathymetry data

To process the water depth from satellite measurements, we suppose that the IOPs are constant in the Arcachon basin inlet at any given time (i.e., for any satellite image).  $r_{rs}^{dp}$  and  $K_d$  are therefore assumed to be constant. This assumption is not fully realistic, but we believe that the error it induces is small

**Table 1** Values of the new coefficients of Eqs. 4, 6, 7, and 9 adjusted to SPOT data. The root mean square error (RMSE) is calculated between the synthetic and inverted parameters using new coefficients and published coefficient (results from the published coefficients are underlined)

Model	Coefficient	Value	RMSE
$r_{rs}$ (Eq. 4)	$n_0$	0.50	0.0008 (0.0012)
	$n_1$	1.90	
$a(\lambda_0)$ (Eq. 9)	$p_0$	0.3202	0.019 (0.049)
	$p_1$	0.2728	
	$p_2$	-0.0249	
$u(\lambda_0)$ (Eq. 6)	$g_0$	0.085	0.0046 (0.0048)
	$g_1$	0.178	
$K_d(\lambda_0)$ (Eq. 7)	$m_1$	3.98	0.045 (0.113)
	$m_2$	0.12	
	$m_3$	11.50	

The reference wavelength is  $\lambda_0=545$  nm

compared with  $NE\Delta r_{rs}$ . In particular, the low value of the signal-to-noise ratio (SNR) of SPOT sensors greatly impacts the detection of small optical changes in the water column. For each image, the mean value at the inlet of  $r_{rs}^{dp}$  and  $K_d$  is calculated following the methodology described in Section 2. The maximum optical water depth,  $H_{max}$ , which represents the depth from which the bottom is no longer “optically” visible by the sensor, is then computed from the following expression:

$$H_{max} = \frac{1}{2K_d} \left[ \ln \left( \frac{1}{\pi} R^B - r_{rs}^{dp} \right) - \ln(NE\Delta r_{rs}) \right] \quad (10)$$

Eq. 10 shows that  $H_{max}$  increases when  $NE\Delta r_{rs}$  decreases and inversely. We can also note that, according to the assumption of a constant bottom albedo, the value of  $R^B/\pi - r_{rs}^{dp}$  is a constant and is always positive due to the high albedo of sandy substratum. The water depth is then processed using Eq. 3 for each pixel for which the value of  $r_{rs} - r_{rs}^{dp}$  is higher than the value of  $NE\Delta r_{rs}$ . Satellite bathymetry is finally computed from the water depth retrieval by removing the tidal elevation provided by the Service Hydrographique et Océanographique de la Marine (SHOM) associated with a given satellite image.

Finally, to validate and evaluate the performances of the QAB, a matchup data set has been created. In this study, matchups refer to acoustic and satellite data that have been collected on the same pixel within a 1-month time interval. One month represents the criterion of temporal proximity. We found 11 satellite images and bathymetric surveys that respect the temporal proximity criterion. Satellite images are composed of one SPOT-2, two SPOT-4, and eight SPOT-5 scenes acquired over different months of year (see Fig. 3). The matchup data set is composed of 43,949 points.

## 4 Results

### 4.1 Bathymetry retrieval from SPOT images

A matchup data set of 43,949 points obtained from 11 satellite images and bathymetric surveys is used to validate and evaluate the performances of the QAB. For these 11 satellite scenes, the value of  $NE\Delta r_{rs}$  varies from 0.0004 to 0.0006  $sr^{-1}$ , which highlights the relatively good radiometric quality of the images. The extracted  $R^B$  and  $r_{rs}^{dp}$  values vary from 0.1790 to 0.2105 and 0.0145 to 0.0180  $sr^{-1}$  with a mean value of 0.1895 and 0.0160  $sr^{-1}$ , respectively. The value of the computed  $K_d$  at 545 nm ranges from 0.32 to 0.79  $m^{-1}$ , with an average value of 0.52  $m^{-1}$ . The range of variability of these parameters is consistent with in situ measurements performed by the authors (unpublished data) and reflects the optical

variability of the water column with respect to the acquisition months of the satellite images. As noted above, the value of  $H_{max}$  depends on the value of  $K_d$ ,  $NE\Delta r_{rs}$ ,  $R^B$ , and  $r_{rs}^{dp}$ . The computed value of  $H_{max}$  varies from 3.10 to 6.95 m, with an averaged value of 4.60 m, which is in agreement with the values measured by Lafon et al. (2002).

The validation of the QAB presented in Section 2 concerns steps 1–4 of the algorithm. For this part of the model, no field data are required. A comparison between the satellite and acoustic water depths extracted from the matchup data set shows relatively good performance, yielding an RMSE and mean absolute bias (AB) value of 1.30 and 1.05 m, respectively. The high value of the bias is explained by an underestimation of the water depth given by the QAB. Analyses of the error and propagation of uncertainties in the model are beyond the scope of this paper and will be performed in another study. However, we believe that the underestimation of the water depth is mainly controlled by the first term of the right-hand expression of Eq. 3 because the impact of the second term is assumed to be negligible in comparison to 1/2 K

To evaluate and compare the performances of the QAB with respect to well-published multispectral methods (Lyzenga et al. 2006, noted L06; Stumpf et al. 2003, noted S03; Dehouck et al. 2012, noted D12), step 5 of the algorithm is now integrated into the satellite water depth processing. The linear regression used to correct the bias observed for the QAB gives values of 1.65 and 0.06 m for  $\alpha$  and  $\beta$ , respectively (see Eq. 8). These values are consistent with the validation results. Figure 4 shows a comparison between the satellite and acoustic water depths for all points in the matchup data set ( $N=43,949$ ). A contour plot is added to the figure to represent the point cloud density. Most of the points are concentrated close to the 1:1 line, indicating good agreement between satellite and acoustic water depth. We note, for low depths, an overestimation of the water depth, which can be explained by a

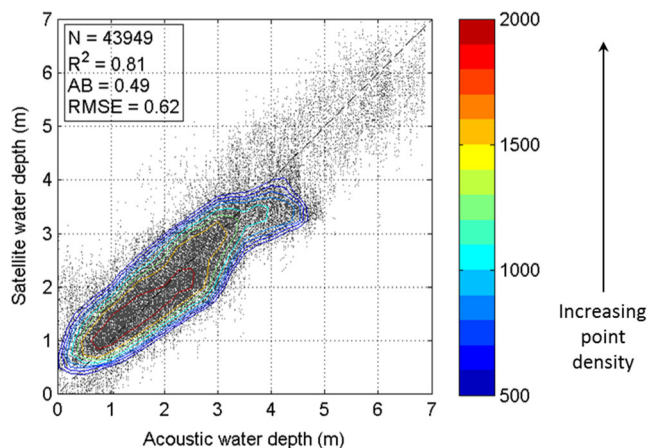


**Fig. 4** Comparison of the satellite and acoustic water depths from the matchup data set ( $N=43,949$ ) associated with 11 SPOT images (from 2001 to 2012). AB is the mean absolute bias, RMSE is the root mean square error, and  $R^2$  is the determination coefficient

relative underestimation of  $K_d$ . For these areas, a higher concentration of suspended sand particles is expected due to strong mixing and resuspension, which could lead to an increase in the  $K_d$  value. For high depths, when  $H$  becomes higher than 4 m, an underestimation of the satellite water depth may be observed. The RMSE and AB values greatly decrease to reach 0.62 and 0.49 m, respectively. The two previously published algorithms, L06 and S03, also perform relatively well, despite their relatively higher RMSE and AB values (1.02 and 0.85 m for L06 and 0.66 and 0.50 m for S03). In contrast, the D12 method shows lower RMSE and AB values (1.31 and 1.15 m, respectively). The poor performance of D12 is directly related to the choice of a time-independent fixed value of  $K_d$  in the model, which cannot be considered a realistic assumption for this coastal environment.

Figure 5 shows an example of bathymetric maps of the Arcachon lagoon inlet produced from a 10-m pixel resolution SPOT-5 image taken on June 24, 2009, at low tide. Figure 5a shows the bathymetric map (projected onto a pixel grid of  $1,600 \times 1,600$ ) associated with the entire area of the Arcachon lagoon inlet. Figure 5b focuses on the UED, located between the northern Cap Ferret sand Spit (CFS) and the UED. Figure 5c focuses on the SDF. For this image, the tidal elevation value is 0.79 m, which allows for accurate bathymetric computations between  $-3.21$  and  $+0.79$  m. Note that the bathymetry in the main channels cannot be estimated because the channel depth ranges from 10 to 20 m. The overall morphology of the inlet and sedimentary entities associated

with this type of mixed energy coastal system is well reproduced and accurately positioned at the pixel level of precision.

These results demonstrate that the QAB applied to high-spatial-resolution multispectral images is robust enough to be used both for quantitative and qualitative morphodynamic studies of mildly to moderately turbid coastal shallow waters. Furthermore, the empirical correction used in the step 5 of the QAB has been established on a large training data set, which can be considered to be statistically representative of the 78 satellite images in terms of optical variability. The QAB can therefore reasonably be applied to the entire satellite archive to investigate the potential of remote sensing to identify long-term trends and quantify decadal changes in the morphology of the Arcachon lagoon inlet.

## 4.2 Large-scale sedimentary features ( $O \sim 100$ m)

### 4.2.1 Quantification of migration rates

Satellite bathymetries retrieved from the QAB show significant changes over the entire Arcachon lagoon inlet during the 26-year period. The long-term migration patterns of the large-scale morphological entities can be described and quantified. In this study, the spatial scale of morphological entities is defined in reference to the spatial resolution of satellite sensors necessary to detect the sedimentary structures. In this section, “large scale” refers to a pixel size with an order of magnitude (noted  $O$ ) of 100 m. As an example, we display the time evolution of the north/south-oriented transect AB (see

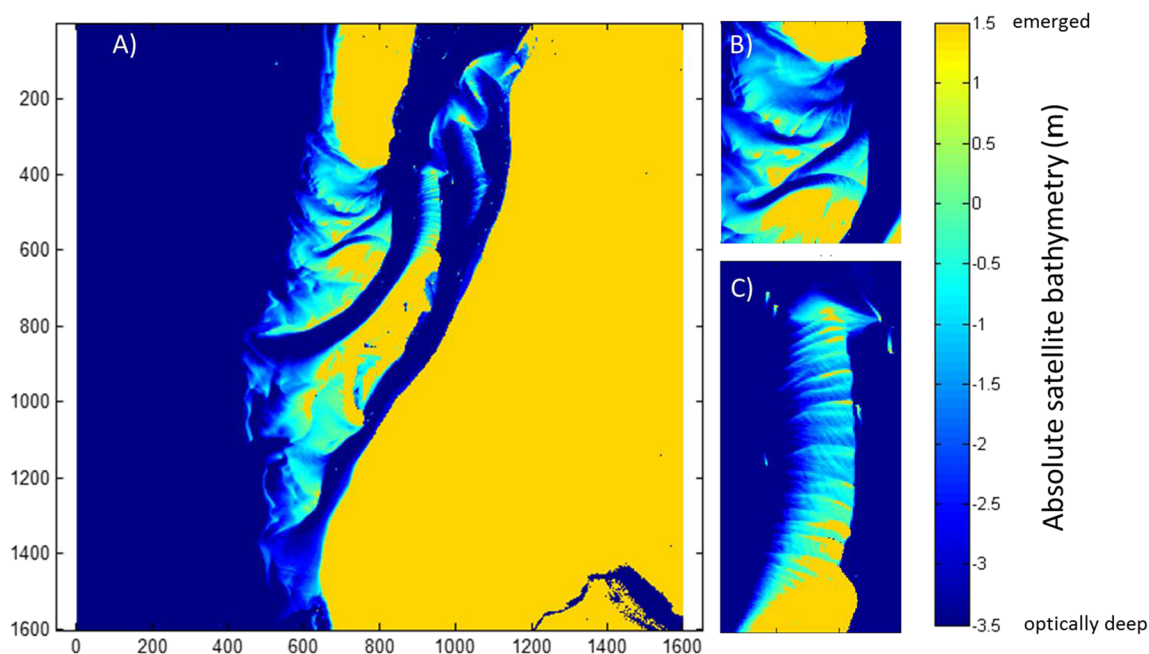


**Fig. 5** Absolute bathymetry (reported in the French Marine Height Datum) processed from a SPOT-5 image (24 June 2009) for **a** the entire area of the Arcachon lagoon inlet, **b** the upper ebb-tidal delta, and **c** the sand dune field

Fig. 2) using the 78 bathymetric maps produced between 1986 and 2012. Figure 6 gives a graphical representation of this evolution with time on the  $x$ -axis and the distance from the CFS along the transect AB on the  $y$ -axis. Dashed lines have been plotted on top of the figure to locate the physical limits of the main sedimentary entities along the transect defined in Section 3.1.

Between 1986 and 2012, the main channels and the downdrift coastline show significant southward migrations, whereas the northern adjacent shoreline, CFS (also called the updrift coast), is subjected to a severe northward regression. Assuming that these morphodynamic behaviors are linear over the time period, migration rates can be roughly estimated by computing the slopes of the lines that represent the position of the sedimentary units as a function of time. NC and SC, which show quasi-time-independent widths, migrate toward the south at 70 ( $\pm 3$ ) and 10 ( $\pm 2$ ) m/year, respectively. The northward regression or erosion of CFS is approximately 17 ( $\pm 2$ ) m/year. Note that because of the different migration rates of NC and SC, the LED width decreases dramatically by a factor of 2 during the period 1986–2012. These migration rates and the general morphological evolution observed in this section are consistent with previous studies (Michel and Howa 1997; Cayocca 2001).

Associated with the dynamics of these main sedimentary entities, Fig. 6 shows the morphological evolution of smaller structures, which characterizes bypassing mechanisms. In particular, in the area of UED, the migration of eight southward sandbars can be observed at an irregular frequency. The migration rate of these sandbars is high, with a mean (standard deviation) of 260 (35) m/year. This is the first time to our knowledge that these large-scale processes have been observed at this spatial and temporal resolution in a mixed energy inlet. A detailed description of the erosion/accretion patterns in UED, which is performed in the next section, is

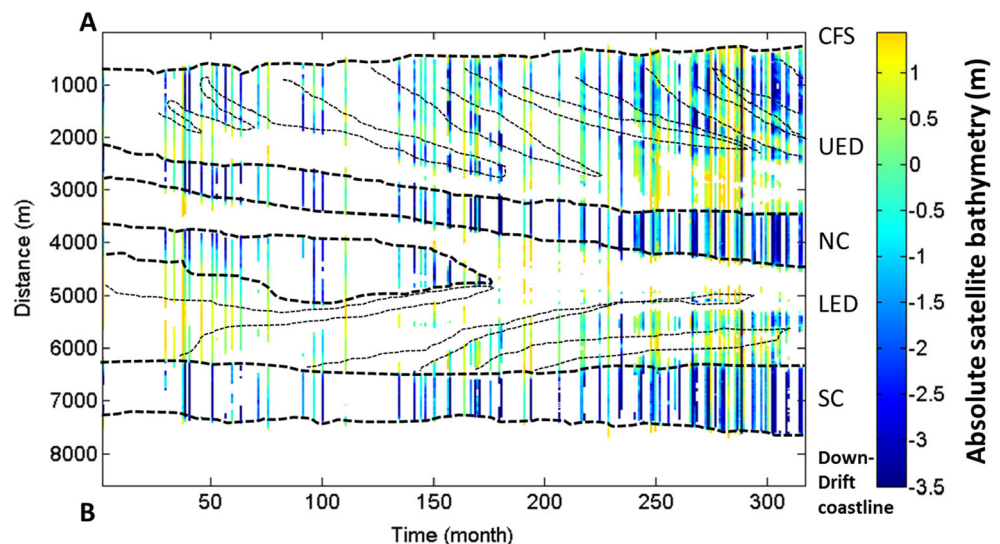
believed to provide further insight into these bypassing mechanisms.

#### 4.2.2 Erosion and accretion patterns

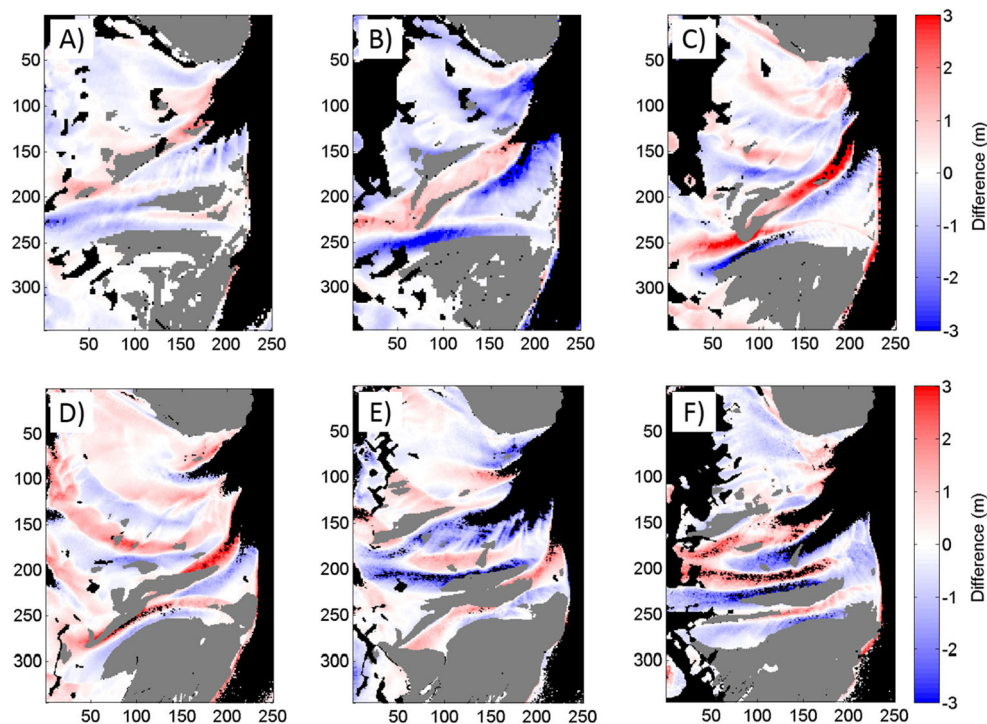
To describe the complex evolution of erosion and accretion patterns in the UED, Fig. 7 displays the annual difference of satellite bathymetry (noted  $\Delta B$ ) for 6 consecutive years (2006–2007, 2007–2008, 2008–2009, 2009–2010, 2010–2011, 2011–2012). This time period corresponds to a complete cycle of the sand supply bypassing the UED from the sandy spit to the southern UED main shoal. For this exercise, satellite images providing similar values of  $K_d$  and comparable ranges of bathymetry have been selected.

Figure 7a shows the erosion/accretion map of the UED produced from satellite data for the period of September 2006 to September 2007. We note an important accumulation of sand ( $\Delta B > +1$  m) at the southern end of the updrift coast and a deepening of the secondary channel ( $\Delta B < -1$  m) located at the northern region of the UED main shoal (white area at the bottom of Fig. 7a). This situation corresponds to the first stage of a sand supply bypassing cycle. Figure 7b, c (associated to the periods September 2007 to October 2008 and October 2008 to June 2009, respectively) displays a southward migration of the sand accumulation area, which acquires a comma shape due to a deflexion of the seaward extent. This deflexion tends to orient the sandbars in the same direction as the NC and generates a counterclockwise rotation of the sedimentary bypassing. Simultaneous to this evolution, an embryonic channel appears at the northern end of the accretion area. During the periods of June 2009 to April 2010 and June 2010 to September 2011 (Fig. 7d, e, respectively), the accumulation area reaches and accretes along the UED main shoal, causing the disappearance of the secondary channel. At the same time, the embryonic channel deepens and becomes a

**Fig. 6** Temporal evolution of the Arcachon lagoon inlet bathymetry on the north/south-oriented transect AB (from the Cap Ferret sand Spit, CFS, to the downdrift coastline; see Fig. 2) obtained by satellite inversion over the period July 1986 to November 2012



**Fig. 7** Erosion/accretion maps of UED from September 2006 to November 2012 projected onto a pixel grid (350×250). The difference in bathymetry (given in m) is computed between **a** September 2006 and September 2007, **b** September 2007 and October 2008, **c** October 2008 and June 2009, **d** June 2009 and April 2010, **e** April 2010 and September 2011, **f** September 2011 and November 2012. *Gray areas* represent the land surfaces. *Pixels in black* are flagged (mainly due to whitecaps or deep waters)



newly formed secondary channel. Figure 7e characterizes the end of the sand supply bypassing cycle. The morphological situation during the period September 2011 to November 2012 (Fig. 7f) is similar to the situation during the period September 2006 to September 2007 (Fig. 7a) in terms of erosion/accretion patterns and characterizes the beginning of a new cycle. Differences with the initial morphological state were characterized, in this case, by a smaller sand accumulation at the southern end of the CFS and a more southern position of the UED main shoal, which presents an additional large sand accretion at the western extent.

#### 4.2.3 Breaching occurrences

Similar bypassing patterns can be observed for the UED and LED sedimentary units with different occurrence frequencies (see Fig. 6). West to northeast-oriented sandbanks located at the seaward extent of the LED experience a general counter-clockwise rotation during their southward migration. This movement, clearly observable on a 2D temporal bathymetric animation (not shown here), induces a massive sand accretion at the southwestern edge of the LED. Bypassing events in the UED are related to breaching mechanisms, which control the opening of new secondary channels. Same mechanisms are observed between the LED and the downdrift coast.

Since the early 1990s, we detected two events of ebb delta breaching in the LED. The first one began in 1991 and lasted approximately 8 years, and the second occurred between 2006 and 2011. Figure 8 shows snapshots of the LED morphology

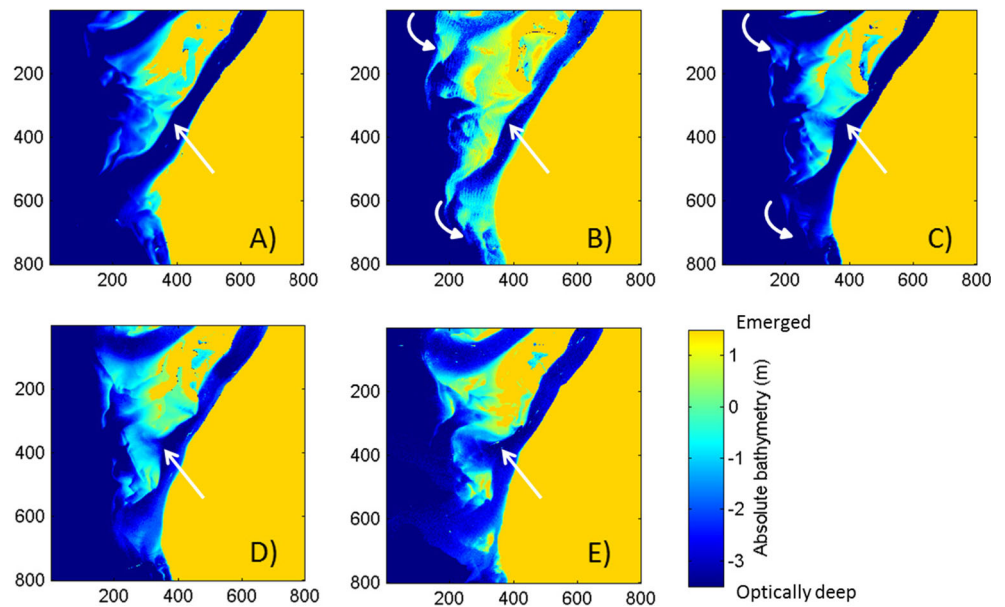
during the second breaching event. Satellite scenes are chosen to highlight the main stages of the sand structure migration process. Figure 8a–e shows the bathymetric maps for 2006, 2008, 2009, 2010, and 2011, respectively.

During the period 2006–2009 (Fig. 8a, c), sandy material bypassed the NC and SC and eventually accreted the LED banks and the downdrift coast, respectively. In the LED, a massive elongated sand accretion is observed in the western part (Fig. 8c, d), while at the same time, the southern edge migrates progressively toward the SC, reducing its width significantly. This sandbank migration occurs with the opening of a new secondary channel, which results from breaching mechanisms. During the period 2010–2011 (Fig. 8d, e), the channel is deepened and splits SC into two mouths. For both the NC and SC, the sand bypassing induces a temporary northward shift of the western part of the channel, whereas the general trend, as shown previously, exhibits a southward migration due to the wave-induced deflection of the sedimentary structures.

#### 4.3 Small-scale sedimentary features (0–10 m)

In the inner part of the inlet, channels are characterized by lower depth values with, in particular, shallow submerged sandbanks at the northern part of the SC. These banks form a flood delta (FD) and are connected to the LED area by a SDF (see Fig. 2). The spatial resolution necessary to detect the SDF and its time evolution is approximately 10 m. As in Section 4.2.1, the long-term migration patterns of these small-

**Fig. 8** Bathymetric maps of the southern part of the Arcachon inlet for **a** September 2006, **b** September 2008, **c** June 2009, **d** April 2010, and **e** September 2011 projected onto a pixel grid (800×800). *Straight white arrows* show the location of the LED breach, and *curved white arrows* represent the sand bypass through both the NC and SC



spatial-scale morphological entities can be described and quantified by analyzing the time evolution of a given transect. Figure 9 gives a graphical representation of the evolution of the transect CD (Fig. 2) with time on the x-axis and the distance measured from the point C on the y-axis. Forty-four bathymetric maps produced between 2004 and 2012 have been used to demonstrate the SDF dynamics. Note that a moving average has been subtracted from the satellite-retrieved bathymetries to focus on the local dune vertical elevation, which has been normalized between 1 and -1. Dune crests and sandy shoals are represented in red, and troughs are represented in blue.

Figure 9 clearly illustrates the migration of the crests and troughs. A general northern migration of the dunes is observed until they reach the southern extent of the FD. Sand dunes present a wavelength of approximately 150 m, with a

magnitude of 3 to 5 m in height. The mean (standard deviation) value of the dune migration rates is 110 (10) m/year. According to Cayocca (2001), the residual tidal current is responsible for the spreading of these hydraulic dunes, allowing for the transfer of the sand originating from the LED to the FD. The SDF additionally shows a slight eastward migration over the period, accompanied by a widening of the NC. Westward-elongated horns of the dune crests also show a counterclockwise rotation during their northward migration, exhibiting sinistral rotation from an N270 along-crest orientation at the southern of the SDF to an N235 orientation at the northern extent. These features tend to support a more active net inward sediment transport along the SC, which accentuates the sinuosity of the along-crest morphology and the counterclockwise rotation of the SDF.

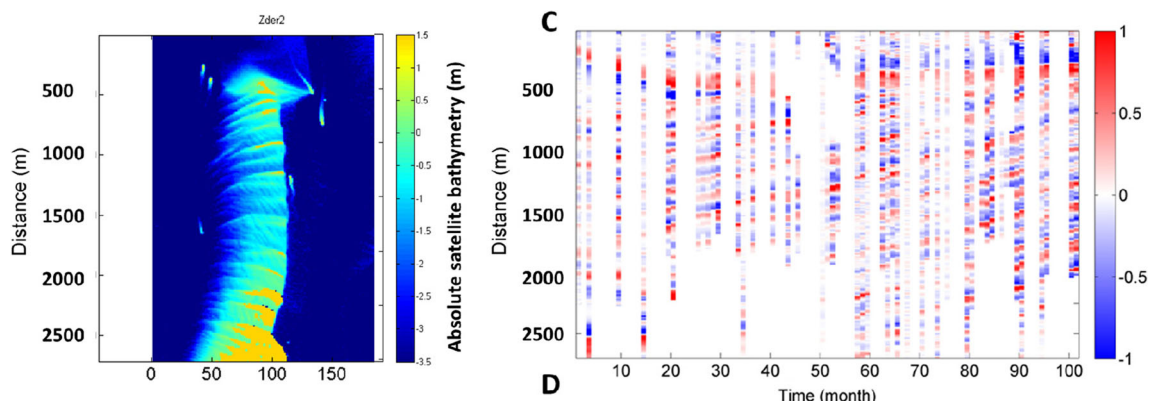


**Fig. 9** The *left panel* represents the bathymetry retrieved from SPOT 5 data (24 June 2009), and the *right panel* represents the temporal evolution of the corrected dune elevation on the north/south-oriented transect CD

(from northern to southern SDF, see Fig. 2) obtained by satellite inversion over the period June 2004 to November 2012

## 5 Global behavior of the inlet

In mixed energy environments, the combined circulation driven by tides and waves induces complex residual circulations and sediment transport. Feedback associated with these environments, which are interactions between hydrodynamics, erosion and deposition processes, and bottom morphology, is poorly documented and understood in comparison to tide-dominated systems. In the past, few experimental and numerical studies focused on the Arcachon lagoon inlet. They showed that the general large-scale evolution of the outer part of the inlet, including the UED and LED, depends on the mean wave regime, whereas the evolution of the inner inlet, including the FD, mainly depends on the tidal asymmetry. They also characterized the sediment transport as a result of the analysis of bypassing and breaching mechanisms.

The long-term observations at high temporal and spatial resolutions achieved in this study, as a result of the analysis of the almost 26-year-long satellite archive of KALIDEOS, allowed the validation of these earlier results. Furthermore, this study provides accurate migration rates of small- and large-scale sedimentary structures and further insight into bypassing and breaching mechanisms. Based on our observations, we propose an updated empirical conceptual model to explain the decadal behavior of the Arcachon lagoon inlet, summarized in Fig. 10. The main sandbanks are represented by blue areas, and sand waves that are transient during bypass processes are shown by gray areas. The positions of the channels are represented by thin and thick gray dotted lines. The thick gray arrow and the thick black arrows represent the WNW wave regime orientation and the littoral drift, respectively. The thin arrows represent the evolution of the sand waves and main sedimentary structures.

The sand material supplied by the net littoral drift reaches the extremity of the CFS and then break away in a WNW-oriented comma-shaped sand wave due to tidal fluxes that deepen embryonic channels and limit their downdrift propagation. The oblique wave action induces a downdrift southward migration of sand waves, which are breached by tidal fluxes to form secondary tidal channels between the CFS and the UED. While migrating downdrift, these sand waves (gray areas on Fig. 10) rotate counterclockwise because the seaward extents are more exposed to the wave regime than the inner part of the sand waves and eventually merge with the main unit of the UED. General trends exhibit a downdrift migration of the ebb delta, primarily composed of two sandbanks and isolating the two main channels. The NC migrates southward with decadal counterclockwise trends, contrasting with the temporary clockwise rotation and updrift of its western end when sand occasionally bypasses from the UED to LED,

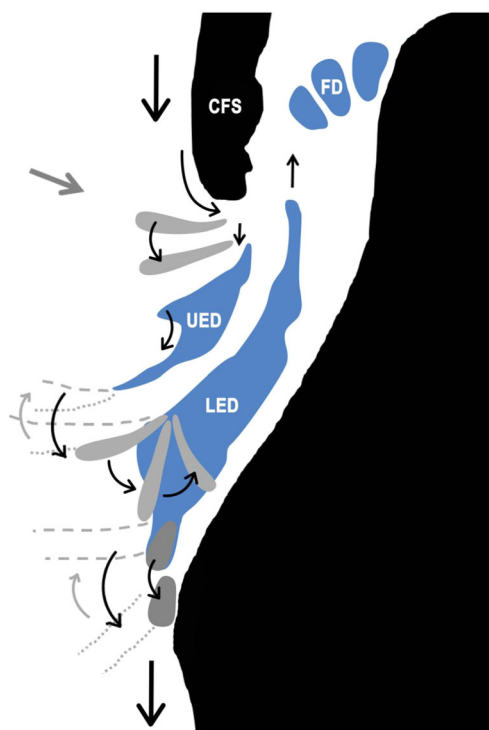


**Fig. 10** Conceptual model of the Arcachon lagoon inlet. *Black areas* represent the updrift and downdrift coastlines; *blue areas*, the ebb and flood deltas; *gray areas*, the sand waves representing the sand bypass processes; *thick gray arrow*, the mean wave direction; *thick black arrows*, the littoral drift direction; *thin arrows*, the evolution of the sedimentary units. The channel orientations are represented by *thin gray dotted lines* (before the sand bypass) and *thick gray dotted lines* (after the sand bypass)

approximately every 6 years (see the shift between the thin and thick dotted gray lines on Fig. 10). The sand bypasses the NC and reaches the LED with an elongated channel-oriented shape that is further constrained by the wave action, combining wave energy dissipation landward with wave refraction, in a counterclockwise rotation of its main unit. Finally, a part of the sediment remobilized by the tidal fluxes in the LED is exported through the inlet and eventually builds the FD by a regular accumulation of sand due to the migration of the SDF.

During the 26-year period, the CFS is subjected to an erosion of 17 m/year, which can be related to the erosive action of the opening and deepening of secondary channels and net sand body release. At the southern end of the CFS, a sand bypass occurs every 2–3 years, with a migration rate of 260 m/year. In the NC and SC, a sand bypass occurs every 6–8 years and decade, respectively. The southward migration of the UED and LED reaches 70 and 10 m/year, respectively. Flood-directed circulation inland induces the migration of sand dune fields northward at a rate of approximately 110 m/year, until they reach the southern limit of the FD. The southern end of the FD migrates southwestward at a rate of 120 m/year since 1986 and increases the meandering of its morphology (not shown here).

## 6 Conclusion

The main objective of this study was to evaluate the potential of satellite-borne ocean color remote sensing to address scientific issues on morphodynamics. For that purpose, an original QAA to estimate the bathymetry, called the QAB, from high-spatial-resolution multispectral sensors (HRS) was developed and validated using a large matchup data set ( $N=43,949$  points). The QAB performs excellently in estimating the depth of mildly to moderately turbid coastal shallow waters in comparison to well-published bathymetry inversion methods. The RMSE and AB values are 0.62 and 0.49 m, respectively, for a  $H_{\max}$  value ranging from 3.10 to 6.95 m.

No field data are required for the QAB, which takes into account the optical variability of the water column. This advantage allows for the exploitation of long-term time series and permits historical morphodynamic approaches. The KALIDEOS-Littoral archive furnished 78 suitable SPOT images, allowing for the analysis of the Arcachon lagoon inlet evolution over a 26-year period (1986–2012) at a seasonal sampling timescale. We demonstrated that HRS are well adapted to analyzing the morphological evolution of small- (i.e., sand dunes), medium- (i.e., sandbanks and channels), and large- (i.e., the entire inlet-lagoon system) scale sedimentary structures. Migration rates of sedimentary entities are quantified, and fundamental mechanisms driving the sediment transport cross the inlet are confirmed. This study confirms and complements the results of previous conceptual and process-based models regarding mixed energy inlets. To conclude, we believe that this study constitutes an important contribution to the understanding and validation of the morphodynamic processes in mixed energy inlet systems as a result of long-term observations acquired at high temporal and spatial resolutions.

**Acknowledgments** This work was supported by the Centre National d'Etude Spatiale (CNES) in the framework of the MORITO project (TOSCA program), INFOLITTORAL-1 project (Pôle de compétitivité-Fonds Unique Interministériel program) and the Region Aquitaine OSQUARII/Inlet project. The authors would also like to thank the CNES and C-S for supplying level-3 data in the frame of the KALIDEOS-Littoral program, the Direction Départementale des Territoires et de la Mer (DDTM) and the Syndicat Intercommunal du Bassin d'Arcachon (SIBA) for supplying the inlet bathymetric soundings data since 2001.

## References

- Albert A, Gege P (2006) Inversion of irradiance and remote sensing reflectance in shallow water between 400 and 800 nm for calculations of water and bottom properties. *Appl Opt* 45(10):2331–2343
- Bertin X, Fortunato AB, Oliveira A (2009) A modeling based analysis of processes driving wave dominated inlets. *Cont Shelf Res* 29(4–5): 819–834
- Bramante JF, Raju DK, Sin TM (2013) Multispectral derivation of bathymetry in Singapore's shallow, turbid waters. *Int J Remote Sens* 34(6):2070–2088
- Butel R, Dupuis H, Bonneton P (2002) Spatial variability of wave conditions on the French Atlantic coast using in situ data. *J Coast Res* SI36:96–108
- Cayocca F (2001) Long term morphological modeling of a tidal inlet: the Arcachon Basin, France. *Coast Eng* 42(2):115–142
- Dastgheib A, Roelvink JA, Wang ZB (2008) Long-term process-based morphological modeling of the Marsdiep Tidal Basin. *Mar Geol* 256:90–100
- De Swart HE, Zimmerman JTF (2009) Morphodynamics of tidal inlet systems. *Ann. Rev. J Fluid Mech* 41:203–229
- Dehouck A, Martiny N, Froidefond JM, Senechal N, Bujan S (2009) New outcomes from spatial remote sensing during the ECORS experiment: towards validation of ocean color products and large-scale bathymetry mapping in a coastal zone. *J Coast Res SI* 56(2):1756–1760
- Dehouck A, Lafon V, Sénéchal N, Froidefond JM, Almar R, Castelle B, Martiny N (2012) Evolution Morphodynamique interannuelle du littoral sud de la Gironde. *Rev Fr de Photogrammétrie et de Télédétection* 197:31–42
- Dekker AG, Phinn SR, Anstee J, Bisset P, Brando VE, Casey B, Fearnly P, Hedley J, Klonowski W, Lee ZP, Lynch M, Lyons M, Mobley C, Roelfsema C (2011) Intercomparison of shallow water bathymetry, hydro-optics and benthos mapping techniques in Australian and Caribbean coastal environments. *Limnol Oceanogr Methods* 9: 396–425
- Dissanayake DMKP, Roelvink JA, Van Der Wegen M (2009) Modelled channel patterns in a schematized tidal inlet. *Coast Eng* 56:1069–1083
- Dongeren AV, Plant N, Cohen A, Roelvink D, Haller MC, Catalan P (2008) Beach Wizard: Nearshore bathymetry estimation through assimilation of model computations and remote observations. *Coast Eng* 55:1016–1027
- Gassiat L (1989) Hydrodynamique et évolution sédimentaire d'un système lagune-flèche littorale : le Bassin d'Arcachon et la flèche du Cap-Ferret. Ph. D. Thesis, Université de Bordeaux
- Gesch DB (2009) Analysis of Lidar elevation data for improved identification and delineation of lands vulnerable to sea-level rise. *J Coast Res SI* 53:49–58
- Gordon HR, Brown OB, Evans RH, Brown JW, Smith RC, Baker KS, Clark DK (1988) A semi-analytical radiance model of ocean color. *J Geophys Res* 93:10909–10924
- Hayes MO (1979) Barrier island morphology as a function of tidal and wave regime. In: Leatherman (Ed.), *Barrier Island*. Academic Press, New York, pp 1–28
- Holman R, Plant N, Holland T (2013) cBathy: a robust algorithm for estimating nearshore bathymetry. *J Geophys Res* 118: 2595–2609
- IOCCG (2006) Remote sensing of inherent optical properties: fundamentals, tests of algorithms, and applications. Lee Z (ed.), *Reports of the International Ocean-Colour Coordinating Group, No. 5*, IOCCG, Dartmouth, Canada
- Kirk J (1991) Volume scattering function, average cosines, and the underwater light field. *Limnol Oceanogr* 36:455–467
- Klemas V (2011) Remote sensing techniques for studying coastal ecosystems: an overview. *J Coast Res* 27(1):2–17
- Lafon V, Froidefond JM, Lahet F, Castaing P (2002) SPOT shallow water bathymetry of a moderately turbid inlet based on field measurements. *Remote Sens Environ* 81:136–148
- Lafrance B, Lenot X, Ruffel C, Cao P, Rabaute T (2012) Outils de prétraitements des images optiques KALIDEOS. *Rev Fr de Photogrammétrie et de Télédétection* 197:10–16
- Lee ZP (2010) Global shallow water bathymetry from satellite ocean color data. *Eos* 91(46):429–430

- Lee ZP, Carder KL, Mobley CD, Steward RG, Patch JF (1999) Hyperspectral remote sensing for shallow waters: II deriving bottom depths and water properties by optimization. *Appl Opt* 38:3831–3843
- Lee ZP, Carder KL, Arnone RA (2002) Deriving inherent optical properties from water color: a multiband quasi-analytical algorithm for optically deep waters. *Appl Opt* 41(27):5755–5772
- Lee ZP, Du KP, Arnone R (2005) A model for the diffuse attenuation coefficient of downwelling irradiance. *J Geophys Res* 110, C02016. doi:10.1029/2004JC002275
- Lyzenga DR (1978) Passive remote sensing techniques for mapping water depth and bottom features. *Appl Opt* 17:379–383
- Lyzenga DR, Malinas NP, Tanis FJ (2006) Multispectral bathymetry using a simple physically based algorithm. *IEEE Trans Geosci Remote Sens* 44(8):2251–2259
- Maritorena S, Morel A, Gentili B (1994) Diffuse reflectance of oceanic shallow waters: influence of water depth and bottom albedo. *Limnol Oceanogr* 39(7):1689–1703
- Michel D, Howa H (1997) Morphodynamic behavior of a tidal inlet system in a mixed-energy environment. *Phys Chem Earth* 22(3–4):339–343
- Minghelli-Roman A, Goreac A, Mathieu S, Spigai M, Gouton P (2009) Comparison of bathymetric estimation using different satellite images in coastal sea waters. *Int J Remote Sens* 30(21):5737–5750
- Mobley CD (1994) *Light and water: radiative transfer in natural waters*. Academic Press
- Nahon A, Bertin X, Fortunato AB, Oliveira A (2012) Process-based 2DH morphodynamic modeling of tidal inlets: a comparison with empirical classifications and theories. *Mar Geol* 291–294:1–11
- O'Neill NT, Miller JR (1989) On calibration of passive optical bathymetry through depth soundings. Analysis and treatment of errors resulting from the spatial variation of environmental parameters. *Int J Remote Sens* 10:148–501
- Pedreiros R, Howa H, Michel D (1996) Application of grain-size-trend analysis for the determination of sediment transport pathways in intertidal areas. *Mar Geol* 135:35–49
- Philpot WD (1989) Bathymetric mapping with passive multispectral imagery. *Appl Opt* 28:1569–1578
- Plecha S, Silva PA, Oliveira A, Dias JM (2012) Establishing the wave climate influence on the morphodynamics of a coastal lagoon inlet. *Ocean Dyn* 62:799–814
- Stumpf RP, Holderied K, Sinclair M (2003) Determination of water depth with high-resolution satellite imagery over variable bottom types. *Limnol Oceanogr* 48(1):547–556
- Su H, Liu H, Heyman WD (2008) Automated derivation of bathymetric information from multi-spectral satellite imagery using a non-linear inversion model. *Mar Geod* 31:281–298
- Van Leeuwen SM, Van Der Vegt M, De Swart HE (2003) Morphodynamic of ebb tidal deltas: a model approach. *Estuar Coast Shelf Sci* 57:899–907
- Viles HA, Goudie AS (2003) Interannual, decadal and multidecadal scale climatic variability and geomorphology. *Earth Sci Rev* 61:105–131
- Wang ZB, Hoekstra P, Burchard H, Ridderinkhof H, De Swart HE, Stive MJF (2012) Morphodynamics of the Wadden Sea and its barrier island system. *Ocean Coast Manag* 68:39–57
- Wettle M, Brando VE, Dekker AG (2004) A methodology for retrieval of environmental noise equivalent spectra applied to four Hyperion scenes of the same tropical coral reef. *Remote Sens Environ* 93: 188–197
- Williams BG, Pan S (2011) Storm-driven morphological evolution and sediment bypassing at a dynamic tidal inlet: a simulation-based analysis. *J Coast Res* SI64:1209–1213
- Woodroffe CD (2003) *Coasts: form, processes and evolution*. Cambridge University Press, Cambridge, 623 pp